Improved Luminescence and Photocatalytic Proprieties of Sm^{3+}-doped ZnO Nanoparticles Via Modified Sol-Gel Route: An Unified Experimental and DFT+U Approach

Sikder Ashikuzzaman Ayon
Bangladesh University of Engineering and Technology
Sajjad Hasan
Bangladesh University of Engineering and Technology
Md Muktadir Billah (mbillah@mme.buet.ac.bd)
Bangladesh University of Engineering and Technology
Sadiq Shahriyar Nishat
Rensselaer Polytechnic Institute (RPI),
Alamgir Kabir
University of Dhaka

Research Article

Keywords: Samarium, XPS, Recombination Rate, Photocatalytic, First Principle, Defect State.

Posted Date: November 17th, 2021

DOI: https://doi.org/10.21203/rs.3.rs-1079490/v1

Abstract

In the current study, a modified sol-gel route was followed to produce undoped and Sm^{3+} doped (1, 3 and 5 mol %) nanoparticles. The study of opto-structural properties of Sm^{3+} doped NPs was carried out both experimentally and theoretically. Complete dissolution of Sm^{3+} ions into the ZnO lattice was obvious from XRD analysis. Morphological evolution with doping was studied using FESEM and TEM. XPS was carried out to confirm the presence of Sm^{3+} on the surface of the doped NPs. Increasing dopant quantity resulted in a red shift of the NPs along with a reduction in band gap with increasing absorption in the visible range, and a minimum of 3.18 eV of optical band gap for $Zn_{0.97}Sm_{0.03}O$ was found. Photoluminescence spectroscopy revealed a drop in the recombination rate of electron-hole with increasing doping till 3 mole %, followed by an increase for $Zn_{0.95}Sm_{0.05}O$. Photogenerated electron-hole pair recombination was revealed by the orange band in the luminescence spectra. Theoretical analysis was also carried out with density function theory (DFT). This work also unfolds the fundamental understanding of the structural properties of the synthesized NPs to enhance photocatalytic activity successfully. Later, photocatalytic activity for the optimum composition i.e., 3 mole percent, was assessed experimentally.

1 Introduction

ZnO nanoparticles (NPs) have gained a lot of popularity in recent years in applications such as UV lasers, photo detectors, gas sensors and photocatalysis which is attributed to the wide direct band gap along with large exciton binding energy [1–4]. Moreover, ZnO nanoparticles have an edge over other semiconductors in optoelectronics due to their non-toxicity, durability along with efficient absorption of the broad solar spectra [5]. Diverse morphology i.e. nanowires, nanorods, nanobelts, nanotubes, nanocapsules and nanohelices has gained considerable popularity among researchers as morphology and sizes play a pivotal role to optimize the optoelectronic properties of ZnO NPs[6, 7]. Additionally, optoelectronic and photocatalytic properties of ZnO NPs can be enhanced through controlled band gap tuning[8–10]. Doping with rare earth elements is a promising approach to tune band gap of ZnO to make it favorable for optoelectronic applications[11–17]. Moreover, rare earth ions delay the recombination of photogenerated charges and thus photocatalytic performance is enhanced by active charge trapping[18]. Furthermore, rare-earth doped ZnO NPs modulate visible region emission because of their unique 4f electronic configuration effectively making them a promising candidate for multicolored LEDs[19–21]. Among rare-earth elements, samarium (Sm) has gained considerable attention among researchers in recent times, because Sm^{3+} ions act as effective luminescent and trapping sites of the charge carriers in ZnO nanoparticles which makes them suitable for optoelectronic and photocatalytic applications[22–24]. Hydrothermal, sol-gel, gaseous phase deposition, successive ionic layer adsorption and reaction (SILAR) method, etc. methods are widely used to synthesize ZnO NPs[25–30]. A pivotal role is played by the synthesizing route to control the morphology, crystallinity and optoelectronic characteristics of the nanoparticles[31]. The modified sol-gel approach has numerous benefits compared to other existing processes, including lower processing costs, simplicity, lower operating temperatures, and improved

control over chemical homogenization of nanoparticles[32]. Here, as the authors believe, for the very first time Sm^{3+} was incorporated in ZnO NPs by this route followed by the experimental study of opto-structural and photocatalytic properties of the synthesized NPs. The DFT study has also been carried out as it has proved to be instrumental in revealing the underlining correlation between structural, opto-electronic properties of rare-earth modified ZnO NPs[33].

2 Methodology

2.1 Synthesis of ZnO NPs Doped with Sm3+

The chemical reagents used in this research were analytical grade. The nanoparticles were prepared by using a required amount of Zinc nitrate hexahydrate and samarium nitrate hexahydrate as precursors. To produce the solution of the salts, de-ionized water was used before the addition of the stabilizer i.e., ethylene glycol. The solution was stirred for an hour while maintaining a temperature of 80°C. The clear homogeneous solution was then supplemented with a double molar amount of citric acid ($C_6H_8O_7$) compared to zinc precursor. The solution was stirred vigorously for two more hours at constant temperature and speed. Meanwhile, the formation of thick gel had occurred and the gel was dried at 120°C. Powders were calcined at 500°C for a couple of hours. Finally, crushed fine powders were obtained by grinding the calcined powders.

2.2 Characterization

The crystal structure of the prepared nanoparticles was investigated by obtaining the powder X-ray diffraction patterns by Philips x-ray diffractometer [PW 3040-X'Pert PRO]. Field emission scanning electron microscopy (FE SEM: JEOL, JSM, 7600F) and transmission electron microscopy (Talos F200X TEM, Thermo Fisher Scientific, USA) were employed to analyze particle morphology and size. SHIMADZU UV 2600 Spectrophotometer was utilized to measure absorbance and diffusion reflectance spectra, with the baseline adjusted with $BaSO_4$ and SHIMADZU RF-6000 Spectro-fluorophotometer (excitation wavelength 200 nm) was employed to examine the photoluminescence (PL) spectra. K-Alpha thermoscientific XPS-spectrometer was used to reveal the chemical states of the species.

2.3 Photocatalytic Degradation

The photocatalytic performance of the NPs under UV light was evaluated by the photodegradation of Rhodamine B (RhB) dye in an aqueous solution of basic medium (pH ~ 10). A solar simulator (Hamamatsu L8288, 500 W) was used to generate solar light and a UV pass filter was used to obtain UV light for the degradation[34–37]. The degradation of the dye under the illumination with the presence of the NPs was measured by the intensity of the absorbance peak of the UV-vis spectroscopy. The absorbance measurement was carried out for 180 min at a 30 min intervals. The stability and reusability test of the nanoparticles was carried out by 4 successive runs. The remaining NPs were extracted from the solution after each cycle to use as photocatalysis in the next photodegradation cycle.

2.4 Computational Analysis

All calculations presented here are based on density functional and done within the project-augmented method. For exchange-correlations, the Perdew-Burke-Ernzerhof (PBE) function was used. In the Generalized gradient approximation (GGA) potential were used for valance electrons of Zn (orbitals: 3d, 4s, 4p), O (orbitals: 2s, 2p) and Sm (orbitals: 4f, 5d) [38]. All the calculations were performed using Quantum Espresso simulation package simulation [39, 40]. The Hubbard-based DFT + U correction scheme was utilized to counter the problem of underestimating band gaps of the standard DFT[41]. This type of correction is used to understand the behavior of compounds made with transition metals [42, 43]. In the DFT (PBE) +U calculations for zinc orbital d, U_{eff} = 10.8eV and for oxygen orbital p, U_{eff} =7eV were used that computed the bandgap of 3.24 eV which is almost similar to the experimentally measured bandgap of pure ZnO. For the f orbital of Sm, we used U_{eff} = 7eV. Rietveld refinement provides the primary structures of the pristine and Sm^{3+} doped ZnO NPs. ZnO has a wurtzite hexagonal structure whose unit cell consists of 2 Zinc and 2 Oxygen atoms. However, for simulating the doped systems, supercells are essential [44, 45]. For structural relaxation plane wave basis was used and pully stress was avoided by energy cutoff at 520 eV. In self-consistent field calculations, between two successive steps the energy convergence benchmark was fixed at 10-7 eV. Relaxation of atomic positions was done to bring Hellmann – Feynman forces below 0.01 eV/Å. Monkhorst-Pack of 12×12×6 scheme and σ = 0.05 sigma value of Gaussian Smearing was used to integrate the Brillouin zone to relax the unit cell. For accurate calculations, tetrahedron smearing method was used where the k-points mesh was 18×18×10. The spin-polarized method was followed for all calculations.

3 Results And Discussion

3.1 X-ray Diffraction

X-ray diffraction data of $Zn_{1-x}Sm_xO$ (x = 0.01, 0.03 and 0.05) NPs are illustrated in figure 1. The data is in accordance with JCPDS card 36-1451 which confirms the hexagonal wurtzite structure of all the nanoparticles [46]. Diffraction peaks of impurity phases such as Sm or Sm_2O_3 were absent which ensures the complete incorporation of Sm^{3+} into the matrix. On doping with Sm^{3+} ions, crystallinity was decreased which is obvious from the reduced diffraction peak intensity. As Zn^{2+} ions ($R_{Zn}{}^{2+}$=0.74 Å) were substituted by Sm^{3+} ions ($R_{Sm}{}^{3+}$=1.09 Å), lattice disorder was generated leading to a decrease in crystallinity [19]. Sm^{3+} doping expands the lattice cell as its radius is larger than that of Zn^{2+}, and therefore, the diffraction peak of the (002) plane shifts subtly towards a lower diffraction angle[47].

For all the planes, Figure 1 shows an increase of full-width half maximum (FWHM) values, which indicates that crystallite size was decreased with increasing dopant amount[48]. Moreover, micro-stain was induced on doping which resulted in lattice disorder and stress generation[49]. Table 1 shows strain and crystallite size values derived from Williamson-Hall (W-H) equation[50–52]. For pristine ZnO average crystallite size was 31.2 nm whereas it was only 11.6 nm for 5 mole percent doping. On the nanoparticle's surface Zn–O–Sm formation impedes further crystal grain growth and thus, decreases the crystallite size [53]. Using Scherrer's equation, the crystallite size was again calculated and a similar trend was

observed[54]. Microstrain increased when dopant was added and maximum microstrain was observed for $Zn_{0.95}Sm_{0.05}O$. Rietveld analysis was done using X'Pert HighScore Plus and the results were summarized in Table 2. Phase purity along with an increase of c/a value from 1.6024 to 1.6037 is confirmed by Rietveld analysis which further supports the low-angle peak shift.

Table 1
Crystallite size, strain and crystallinity of pristine and doped ZnO NPs

Element	Crystallite Size (nm)		Strain, $\varepsilon * 10^{-3}$
	W-H plots	Scherrer's Equation	(W-H plots)
ZnO	31.2	28.4	0.82
$Zn_{0.99}Sm_{0.01}O$	22.5	18.1	1.95
$Zn_{0.97}Sm_{0.03}O$	16.9	15.2	2.16
$Zn_{0.95}Sm_{0.05}O$	11.6	12.3	3.04

Table 2
Rietveld analysis of pristine and doped ZnO NPs

Element	Lattice Parameters (Å)			Profile Factor, R_p	Weighted Profile Factor, R_{wp}	Goodness of Fit
	a	c	c/a			
ZnO	3.2495	5.2072	1.6024	6.53	8.84	1.79
$Zn_{0.99}Sm_{0.01}O$	3.2502	5.2089	1.6026	7.04	9.32	1.92
$Zn_{0.97}Sm_{0.03}O$	3.2493	5.2103	1.6035	5.75	7.63	1.56
$Zn_{0.95}Sm_{0.05}O$	3.2483	5.2092	1.6037	5.08	6.44	1.31

3.2 Morphology of Nanoparticles

With increasing doping amount, a smaller-size morphology was evolved compared to pristine ZnO nanoparticles (figure 2). Hexagonal nanoparticles for undoped ZnO were observed which is evident from figure 2a. When Sm^{3+} replaces Zn^{2+} in nanoparticles, it induces a positive charge, which affects the morphology[55]. Nanoparticles' size showed a decrease when dopant amount raises from 1 mole to 3 mole percent as particle growth is inhibited on doping(figure 2(b-c))[56]. An increase in the size of nanoparticles was observed for further doping and the shape of the nanoparticles become near-spherical along with agglomerated nanoparticles (figure 2d).

The variation in particle size with doping was also clearly visible in TEM images (figure 3). The particle size of hexagonal-shaped undoped ZnO NPs varied from 40 to 60 nm, with occasional outliers (figure 3(a-b)). In $Zn_{0.97}Sm_{0.03}O$ nanoparticles, small-sized homogeneous nanoparticles ranging from 20 to 25 nm were observed (figure 3(a-b)). The findings are analogous to those of XRD and FESEM.

3.3 UV-vis Spectroscopy

$Zn_{1-x}Sm_xO$ (x = 0.01, 0.03 and 0.05) NPs showed a decrease in reflectance in UV-vis spectra which is shown in figure 4a. The light was scattered by grain boundaries of smaller-sized doped NPs which reduces reflectance[19]. Figure 4b illustrates the strong absorption threshold of pristine and doped NPs near 370 nm. The absorption edge widens as doping was increased and shifts to higher energy. Red shift and enhanced visible light absorption ability were observed with increasing concentration due to the narrower band gap. In this case, electron and hole are transferred between 4f orbital of Sm ion and ZnO valence or conduction band[57, 58]. For $Zn_{0.95}Sm_{0.05}O$, absorption in the visible region was slightly decreased as further doping is responsible for surface defects. Kubelka-Munc formula was used for calculating band gaps and are listed in Table 3[59]. $Zn_{0.97}Sm_{0.03}O$ showed least band gap of 3.18 eV which is created by excessive energy surfaces between conduction and valence bands of ZnO compared to others (figure 5)[60]. Due to the Moss-Burstein effect further doping increased the band gap, pointing out that low energy transitions are blocked as with increasing dopant concentration, fermi level within conduction bands moves upward[61, 62]. From the theoretical study discussed later, it is found that band gap decreases on 5 mole percent doping. Though the trend of experimental band gap contradicts with the trend of computational band gap beyond 3 mole percent doping, a similar trend is found when the impurity states were taken into account.

3.4 Photoluminescence Spectroscopy (PL)

Photoluminescence spectra were studied for understanding the defect states and presented in figure 6. Near band emission (NBE) is appeared as a sharp peak in the UV area as a result of excitonic non-radiative recombination[19]. Emission wavelengths were used to calculate band gap which were quite similar to the band gaps measured by the Kubelka-Muck function and is represented in Table 3. Deep level emissions (DLE) were represented by the broad orange peaks near 600 nm[19, 63]. Oxygen interstitial (O_i^{2-}) defects were created while doping to maintain charge balance which is represented by: $3Zn^{2+} = 2Sm_{Zn}^{3+} + Zn^{2+} + O_i^{2-}$ [19, 64]. Radiative recombination amid metastable states leads to strong orange luminescence. Photo-generated electron-hole recombination rate was mitigated resulting in decreased orange peak intensity up to 3 mole percent addition[53, 65]. However, as dopant concentration increases beyond 3 mole percent, the recombination rate was increased slightly which was evident from the marginal increase in the peak intensity (figure 6). As defects increase with increasing dopant concentration, they might become a center for recombination in $Zn_{0.95}Sm_{0.05}O$[66]. Defect annihilation or larger particle size (figure 2d) where recombination can take place before charge carriers reach particle surface, can also be responsible for the increased peak intensity[67].

3.5 X-ray Photoelectron Spectroscopy (XPS)

Figure 7a shows survey scans of ZnO and $Zn_{0.97}Sm_{0.03}O$ NPs. The survey scan of ZnO reveals the presence of Zn, O and C. Either CO/CO_2 absorption in the surface or air contamination is responsible for C1s peak[66]. Two peaks of Sm are found in the survey scan of $Zn_{0.97}Sm_{0.03}O$. From the high resolution

scan of Zn 2P of ZnO, the difference in binding energy between Zn 2p1/2 (1044.69 eV) and Zn 2P3/2 (1021.64 eV) is found around 23.05 eV which confirms that Zn is present in Zn^{2+} oxidation state (figure 7b)[68]. When Sm is added, this difference changes slightly to around 23.11 eV and both Zn 2p1/2 (1044.45 eV) and Zn 2P3/2 (1021.34 eV) peaks shift to lower binding energies corresponds to the electronic interactions of Sm with the lattice (figure 7b)[68]. Figures 7c and 7d represent the scan of O 1s of ZnO and $Zn_{0.97}Sm_{0.03}O$, respectively. From the deconvolution of the O 1s peak, three distinct fitted peaks are observed in both cases. The fitted peaks at around 530.13 eV for ZnO and 529.94 eV for $Zn_{0.97}Sm_{0.03}O$ represent the presence of lattice Oxygen [69]. The absorbed oxygen on the surface attributes to the peaks at around 531.66 eV and 531.46 eV in ZnO and $Zn_{0.97}Sm_{0.03}O$, respectively[66]. The other peak at 533.14 eV in ZnO and 532.40 eV in $Zn_{0.97}Sm_{0.03}O$ corresponds to the absorbed hydroxyl species from water[69]. It is evident from figure 7e that two peaks of Sm 3d3/2 and Sm 3d5/2 are present at around 1110.27 eV and 1083.29 eV, respectively. These peaks confirm the presence of Sm3+ in the lattice structure[70]. The absence of other peaks of Sm further confirms that Sm is only present in the trivalent state and no secondary phase of Sm_2O_3 is present in the lattice[71].

Table 3
Comparison of band gap calculated in different methods.

Element	Calculated Band Gap (eV)		
	From Kubelka-Muck Function	From PL spectra	From DFT Calculation
ZnO	3.25	3.14	3.24
$Zn_{0.99}Sm_{0.01}O$	3.23	3.14	3.19
$Zn_{0.97}Sm_{0.03}O$	3.18	3.12	3.12
$Zn_{0.95}Sm_{0.05}O$	3.22	3.13	3.06

3.6 Photocatalytic Degradation Test

ZnO and $Zn_{0.97}Sm_{0.03}O$ NPs were taken to perform the degradation test of a standard dye, RhB, using the visible light filter. $Zn_{0.97}Sm_{0.03}O$ NPs are selected as the optimum concentration among doped products as these NPs exhibit a lower recombination rate of photogenerated electron-hole pairs along with the least band gap which is essential for photocatalytic activity[64]. It is evident from figure 8(a, b) that with UV radiation, the absorption peak of RhB dye decreased steadily for both the nanoparticles. After 3 hours' irradiations under UV-light, 56% and 80% degradation were observed for ZnO and $Zn_{0.97}Sm_{0.03}O$, respectively. Figure 8(c) shows superior degradation was found for $Zn_{0.97}Sm_{0.03}O$ NPs. This is because of the lower recombination rate of photo-generated charge carriers. The particles were smaller which is also favorable for photocatalytic reactions as the surface area to volume ratio is higher for $Zn_{0.97}Sm_{0.03}O$ than pristine ZnO nanoparticles[32, 58, 64, 72]. The kinetic equation of Langmuir-Hinshelwood (L-H) can be used to model the degradation of several dyes by heterogeneous semiconductors used as photocatalysts[73]. Equation 1 is applicable when the initial concentration is low.

$$\ln \frac{c_0}{c} = Kt \quad (1)$$

Here, C_o is the original concentration of organic dye at t=0. The final concentrations at t = t is C. K is the apparent first-order rate constant. Pristine and $Zn_{0.97}Sm_{0.03}O$ nanoparticles showed a linear relationship when $\ln(C_o/C)$ was plotted against time which is presented in figure 8(d). K was calculated 0.00435 min^{-1} and 0.00852 min^{-1} for pure and $Zn_{0.97}Sm_{0.03}O$, respectively. 1.95 times higher rate of degradation was found for $Zn_{0.97}Sm_{0.03}O$ nanoparticles compared to pristine ZnO NPs. Figure 8(e) illustrates the recyclability test of $Zn_{0.97}Sm_{0.03}O$ nanoparticles under identical test conditions. After four consecutive cycles, degradation efficiency slightly decreased under similar experimental condition. This happens due to the slight loss of nanoparticles during recycling. Figure 8(f) shows a visual representation of the continual discoloration of RhB dye to degradation caused by $Zn_{0.97}Sm_{0.03}O$ nanoparticles under UV illumination.

Sm^{3+} possesses the ability to separate photogenerated electron-hole pairs which is evident by photoluminescence spectra where all the Sm^{3+} doped ZnO NPs showed a lower electron-hole recombination rate compared to pristine. Thus, reactive species such as hydroxyl radicals (OH•), superoxide anion radicals ($O_2^{\bullet -}$) could be generated when samarium is introduced into the ZnO matrix. [64, 74] Sm^{3+} having partially filled f-elections can mitigate electron-hole recombination by trapping electrons of the conduction band which is produced by irradiation.[58, 75] Unstable Sm^{2+} can easily transfer this electron to produce superoxide anion racial followed by producing hydroxyl radicles in subsequent steps. These active OH• radicals react with RhB and decompose it[36]. This mechanism is postulated in figure 9 and the related reactions are listed below:

$ZnO + h\nu \rightarrow ZnO\ (e^-_{(CB)}) + (h^+_{(VB)})$

$Sm^{3+} + e^-_{(CB)} \rightarrow Sm^{2+}$ (Trapping of electron)

$Sm^{2+} + O^2 \rightarrow Sm^{3+} + O_2^{\bullet -}$ (Transfer of electron)

$O_2^{\bullet -} + H^+ \rightarrow OOH\bullet$

$OOH\bullet + H^+ + e^-_{(CB)} \rightarrow H_2O_2$

$H_2O_2 + e^-_{(CB)} \rightarrow OH\bullet + OH^-$

$RhB + OH\bullet \rightarrow Intermediates \rightarrow CO_2 + H_2O$

Furthermore, photogenerated holes could also produce hydroxyl radicles by reacting with water molecules on the surface of the catalysts which may also take part in the degradation process by the following reactions:

$h^+_{(VB)} + H_2O \rightarrow H^+ + OH\bullet$

$h^+_{(VB)} + OH^- \rightarrow OH\bullet$

3.7 First principle analysis using DFT

For calculating the different properties from DFT for different Sm^{3+} concentrations in ZnO, supercells have been built having various sizes. 4x4x3, 3x3x2 and 3x3x1 supercells of ZnO are used as models for 1.04, 2.80 and 5.50 mole% Sm^{3+} doping, respectively and presented in figure 10(a-d). They are the closest doping percentages possible for Sm^{3+} doping which is comparable to experimental studies viz. for mole percentages 1, 3 and 5. As the atomic radius of dopant and host lattice atoms varied, crystal structures changes differently. Lattice parameters for pure ZnO are calculated by DFT analysis and found to be a=b= 3.28 Å and c=5.30 Å. When DFT+U approach was employed a slight change in lattice parameter is observed where a=b= 3.05 Å and c= 4.92 Å. These values are analogous to the experimentally-calculated parameters as well as the parameter calculated by the DFT and DFT+U approach in previous studies of ZnO[45, 76].

The bond length changes greatly near the doping positions as the radius of Sm^{3+} ion is greater than that of Zn^{2+} ion, which may be ascribed to the difference of the atomic radius and the number of valence electrons between dopants and the host atoms. The bond lengths of pristine and doped ZnO NPs are listed in Table 4. From the relaxed structure, it is revealed that the crystal structure shows some distortion after doping which is localized only around the impurity atom. The Sm-O bond length increased progressively with increasing doping. Due to this increasing bond length, the lattice constant (c/a) is also increasing with the doping concentrations of Sm^{3+} which is evident from XRD analysis. As Sm^{3+} ions turn out to be more closely space out for increasing doping, greater impurity-impurity contact expanded the bond length. This also affects electronic properties.

Table 4
Bond lengths of undoped and doped ZnO NPs.

Element	Bond length (Zn-O) near Sm atom	Bond length (Sm-O)
ZnO	2.001 Å(DFT), 1.87 Å (DFT+U)	N/A
$Zn_{0.99}Sm_{0.01}O$	1.87 Å (DFT+U)	2.26 Å (DFT+U)
$Zn_{0.97}Sm_{0.03}O$	1.87 Å ((DFT+U)	2.27 Å (DFT+U)
$Zn_{0.95}Sm_{0.05}O$	1.88 Å (DFT+U)	2.31 Å (DFT+U)

From calculation, a direct bandgap of 0.72 eV is found at Γ point (figure 11a). This is much less significant than the investigational value of 3.25 eV. Often standard DFT underestimates bandgap of ZnO. So effective on-site Coulomb interaction (U) (DFT + U) was used with density functional theory (DFT). Usually, standard Kohn–Sham eigenvalues exclude quasiparticle energies. So, the inadequate

treatment of quasi-core electrons of a deeply correlated structure like ZnO which leads to a strong p-d hybridization. This is a very common issue for many strongly correlated systems.

The value for Ueff as 10.8 eV for zinc d orbital and 7 eV for oxygen p orbital was used. Thus, a direct band gap of 3.25 eV was calculated which is comparable to the value of 3.25 eV, which was found experimentally (figure 11b). But the reduction in the bond length along with lattice parameters was measured. The localization of the d-state reduced the lattice constant which further drags the electron toward the core. For the rest of the calculations, these U_{eff} values were used.

The spin-polarized DOS and band structure for different doping concentrations of Sm^{3+} were calculated. The calculated projected density of states (PDOS) for the nanoparticles as a function of energy is plotted in figure 12. The valance band of undoped ZnO is created by firmly hybridized O 2p and Zn 3d orbitals. Here, the impact from O 2p orbital is greater. From the color gradient in figure 12, it is evident that the conduction band minima (CBM) is composed of orbitals of both Zn and O atoms. There is no atomic magnetization is observed for pure ZnO as evident from the symmetric DOS. Later, magnetization was calculated as zero for this calculation. The upper valence band of doped ZnO from -2.5 eV to approximately -7.5 eV originates primarily from the O 2p and Zn 3d orbitals. As Sm^{3+} has more valence electrons than Zn^{2+}, with doping the system becomes more n-type. Here, fermi level moves towards the conduction band for all three doped cases. Interestingly, Sm^{3+} has introduced some impurity states from Sm 4f orbital in the gap region. Sm 4f and 5d orbitals in the conduction band also contribute to a little extent in addition to Zn and O atom orbitals.

Contribution from Sm 4f and 5d orbitals near the conduction band region is visible from the PDOS where the contribution from Sm 5d orbitals is more prominent. So, the Sm 5d and Sm 4f orbitals are responsible for the change in the bandgap. Sm 5d orbitals pushed the conduction band region towards Fermi level. This makes the bandgap smaller as doping concentration increases gradually. Figure 13(a-c) represents the band structure of Sm^{3+} doped ZnO NPs with increasing dopant concentration. From the DFT calculation band gap is calculated as 3.19, 3.12 and 3.06 eV for 1.04, 2.8, and 5.5 mole % doping, respectively. All values correspond to the experimental findings to show the trend of band gap tuning up to 3 mole percentage addition. However, for 5 mole percent doing the trend is different from experimental and DFT results. Consideration of the impurity states caused by doping can explain this difference.

In the case of 1.04% doping, there are some impurity states introduced in the middle of the bandgap region. These impurity states are originated from Sm 4f orbitals. As the concentration of Sm^{3+} increased, more states are introduced in the bandgap region. However, impurity orbitals are found under Fermi level i.e., these states can be occupied by electrons. As a result, these impurity states must have some significant effect on bandgap. If the bandgap is considered from the upper edges of the impurity states to the lower edge of conduction band minima, bandgap change with a similar trend to the experimental results is found. From this calculation 0.67, 0.48 and 0.75 eV bandgap are found for 1.08, 2.8 and 5.5 mole percent doping, respectively. Thus, the minimum band gap was found for 2.8 mol % dopant concentration which follows the findings of experimental results. So, the dopant concentrations i.e.,

impurity states play a major role in bandgap tuning. These band gap values are quite different than those band gaps obtained experimentally since the defect states are created at a deep level, however, this shows that because of defect states band gap may decrease experimentally for 5 mole percent doping.

For both 1.04 and 5.5 mole percent doping, the localized impurity states were formed very near to Fermi level. The trapped states serve as the recombination centers for charge carriers. But the scenario is different for 2.8 mole % dopant concentration as the impurity states are not that much localized and are well spaced spreading in between the Fermi level and valence band maxima (VBM). These states can act as hole trapping sites that can reduce the carrier recombination rates. This result is shown well agreement with the PL observations and suggests that photocatalytic performance should be best for 3 mole percent doping. However, photocatalytic degradation was investigated only for $Zn_{0.97}Sm_{0.03}O$ among the doped ZnO considering the fact that PL study showed minimum recombination rate of charge carriers for 3 mole percent doping and no significant change in band gap was observed for further doping beyond this doping concentration.

4 Conclusion

$Zn_{1-x}Sm_xO$ (x = 0.01, 0.03 and 0.05) NPs were produced by a modified sol-gel route followed by a comprehensive analysis focusing on structural and optical characteristics. No peaks for the extra phase was present in XRD which confirms the complete dissolution of Sm^{3+} into the lattice. Moreover, the presence of trivalent Sm^{3+} in XPS further confirms that there was no secondary phase of Sm_2O_3. On doping, particles became smaller up to 3 mole percent dopant concentration. It was observed that Sm^{3+} doping effectively enhanced the visible light absorbability of ZnO NPs along with red shift and the least band gap of 3.18 eV was observed for 3 mole percent doping. Moreover, Sm^{3+} doping facilitates radiative recombination of photogenerated holes and electrons and thus produces an orange band in the spectrum. It is evident from PL that the lowest recombination rate was observed for $Zn_{0.97}Sm_{0.03}O$ NPs which makes it favorable for photocatalytic applications. $Zn_{0.97}Sm_{0.03}O$ NPs showed 1.95 times greater degradation of RhB dye compared to pristine ZnO NPs because of its low recombination rate and smaller-sized particles with a high surface to volume ratio. Finally, the DFT study showed that calculated band gap values are comparable with experimental findings with a similar trend up to 3 mole percent dopant addition and consideration of the defect states created by doping can predict band gap changing trend for further doping beyond this dopant concentration. DFT study also predicts the lowest recombination rate for $Zn_{0.97}Sm_{0.03}O$ which agrees well with the results found from PL spectra and suggests the highest photocatalytic performance for this dopant concentration.

Declarations

CONFLICTS OF INTEREST

There are no conflicts of interest to declare.

Acknowledgements

The authors would like to express their gratitude to Committee of Advanced Studies and Research (CASR) and department of Materials and Metallurgical Engineering (MME), Bangladesh University of Engineering and Technology (BUET) for the assistance. Authors are also grateful to Dr. Mohammed Abdul Basith, Professor, Department of Physics, BUET, for his PL and photocatalytic setup facilities.

References

1. A.B. Djuriić, A.M.C. Ng, X.Y. Chen, ZnO nanostructures for optoelectronics: Material properties and device applications. Prog. Quantum Electron. **34**, 191–259 (2010)
2. R.D. Suryavanshi, S.V. Mohite, A.A. Bagade, S.K. Shaikh, J.B. Thorat, K.Y. Rajpure, Nanocrystalline immobilised ZnO photocatalyst for degradation of benzoic acid and methyl blue dye. Mater Res Bull **101**, 324–333 (2018). https://doi.org/10.1016/j.materresbull.2018.01.042
3. L. Zhu, W. Zeng, Y. Li, New insight into gas sensing property of ZnO nanorods and nanosheets. Mater Lett **228**, 331–333 (2018). https://doi.org/10.1016/J.MATLET.2018.06.049
4. M. Hjiri, F. Bahanan, M.S. Aida, L. El Mir, G. Neri, High Performance CO Gas Sensor Based on ZnO Nanoparticles. J Inorg Organomet Polym Mater 2020 **3010 30**, 4063–4071 (2020). https://doi.org/10.1007/S10904-020-01553-2
5. C.B. Ong, L.Y. Ng, A.W. Mohammad, A review of ZnO nanoparticles as solar photocatalysts: Synthesis, mechanisms and applications. Renew. Sustain. Energy Rev. **81**, 536–551 (2018). https://doi.org/10.1016/j.rser.2017.08.020
6. M. Faisal, A.A. Ismail, A.A. Ibrahim, H. Bouzid, S.A. Al-Sayari, Highly efficient photocatalyst based on Ce doped ZnO nanorods: Controllable synthesis and enhanced photocatalytic activity. Chem. Eng. J. **229**, 225–233 (2013). https://doi.org/10.1016/j.cej.2013.06.004
7. A. Mahana, O.I. Guliy, S.C. Momin, R. Lalmuanzeli, S.K. Mehta, Sunlight-driven photocatalytic degradation of methylene blue using ZnO nanowires prepared through ultrasonication-assisted biological process using aqueous extract of Anabaena doliolum. Opt. Mater. (Amst) **108**, 110205 (2020). https://doi.org/10.1016/J.OPTMAT.2020.110205
8. S.C. Das, R.J. Green, J. Podder, T.Z. Regier, G.S. Chang, A. Moewes, Band gap tuning in ZnO through ni doping via spray pyrolysis. J. Phys. Chem. C **117**, 12745–12753 (2013). https://doi.org/10.1021/jp3126329
9. A. Saboor, S.M. Shah, H. Hussain, Band gap tuning and applications of ZnO nanorods in hybrid solar cell: Ag-doped verses Nd-doped ZnO nanorods. Mater. Sci. Semicond. Process. **93**, 215–225 (2019). https://doi.org/10.1016/j.mssp.2019.01.009
10. N. Ben Saber, M. Ibrahim, A. Mezni, M.M. Ibrahim, A.A. Shaltout, M. Mersal, G.A. Mostafa, N.Y. Alharthi, S. Boukherroub, R. Altalhi, T. Pt-ZnO/M (M = Fe, Co, Ni or Cu): A New Promising Hybrid-Doped Noble Metal/Semiconductor Photocatalysts. https://doi.org/10.1007/s10904-020-01588-5

11. M. Achehboune, M. Khenfouch, I. Boukhoubza, B.M. Mothudi, I. Zorkani, A. Jorio, Holmium (Ho)-coated ZnO nanorods: an investigation of optoelectronic properties. J Mater Sci Mater Electron **31**, 4595–4604 (2020). https://doi.org/10.1007/s10854-020-03011-8
12. V. Anand, A. Sakthivelu, K.D.A. Kumar, S. Valanarasu, A. Kathalingam, V. Ganesh, M. Shkir, S. AlFaify, I.S. Yahia, Rare earth Sm3+ co-doped AZO thin films for opto-electronic application prepared by spray pyrolysis. Ceram. Int. **44**, 6730–6738 (2018). https://doi.org/10.1016/j.ceramint.2018.01.088
13. V.H.T. Thi, B.K. Lee, Effective photocatalytic degradation of paracetamol using La-doped ZnO photocatalyst under visible light irradiation. Mater Res Bull **96**, 171–182 (2017). https://doi.org/10.1016/j.materresbull.2017.04.028
14. I.L. Poul Raj, S. Valanarasu, K. Hariprasad, J.S. Ponraj, N. Chidhambaram, V. Ganesh, H.E. Ali, Y. Khairy, Enhancement of optoelectronic parameters of Nd-doped ZnO nanowires for photodetector applications. Opt. Mater. (Amst) **109**, 110396 (2020). https://doi.org/10.1016/J.OPTMAT.2020.110396
15. C. Selvaraju, R. Karthick, R. Veerasubam, The Modification of Structural, Optical and Antibacterial Activity Properties of Rare Earth Gadolinium-Doped ZnO Nanoparticles Prepared by Co-Precipitation Method. J Inorg Organomet Polym Mater 2018 **293 29**, 776–782 (2018). https://doi.org/10.1007/S10904-018-1051-0
16. T. Ghrib, I. Massoudi, A.L. Al-Otaibi, A. Al-Malki, A. Kharma, E. Al-Hashem, R.A. Al-Ghamdi, R.A. Al-Zuraie, Effects of Terbium Doping on Structural, Optical and Photocatalytic Properties of ZnO Nanopowder Prepared by Solid-State Reaction. J Inorg Organomet Polym Mater 2020 **311 31**, 239–250 (2020). https://doi.org/10.1007/S10904-020-01761-W
17. J. El Ghoul, F.F. Al-Harbi, Synthesis, Structural and Optical Properties of Er and V Codoping ZnO Nanoparticles. J Inorg Organomet Polym Mater 2020 **311 31**, 272–278 (2020). https://doi.org/10.1007/S10904-020-01678-4
18. M. Khatamian, A.A. Khandar, B. Divband, M. Haghighi, S. Ebrahimiasl, Heterogeneous photocatalytic degradation of 4-nitrophenol in aqueous suspension by Ln (La 3+, Nd 3+ or Sm 3+) doped ZnO nanoparticles. J Mol Catal A Chem **365**, 120–127 (2012). https://doi.org/10.1016/j.molcata.2012.08.018
19. D. Arora, K. Asokan, A. Mahajan, H. Kaur, D.P. Singh, Structural, optical and magnetic properties of Sm doped ZnO at dilute concentrations. RSC Adv **6**, 78122–78131 (2016). https://doi.org/10.1039/c6ra12905f
20. Q. Luo, L.S. Wang, H.Z. Guo, K.Q. Lin, Y. Chen, G.H. Yue, D.L. Peng, Blue luminescence from Ce-doped ZnO thin films prepared by magnetron sputtering. Appl. Phys. A Mater. Sci. Process. **108**, 239–245 (2012). https://doi.org/10.1007/s00339-012-6883-9
21. C. Jayachandraiah, K. Siva Kumar, G. Krishnaiah, N. Madhusudhana Rao, Influence of Dy dopant on structural and photoluminescence of Dy-doped ZnO nanoparticles. J. Alloys Compd. **623**, 248–254 (2015). https://doi.org/10.1016/j.jallcom.2014.10.067

22. M. Faraz, F.K. Naqvi, M. Shakir, N. Khare, Synthesis of samarium-doped zinc oxide nanoparticles with improved photocatalytic performance and recyclability under visible light irradiation. New J Chem **42**, 2295–2305 (2018). https://doi.org/10.1039/c7nj03927a
23. P. Sukriti, Chand, V. Singh, Enhanced visible-light photocatalytic activity of samarium-doped zinc oxide nanostructures. J. Rare Earths **38**, 29–38 (2020). https://doi.org/10.1016/j.jre.2019.02.009
24. M.M. Ba-Abbad, M.S. Takriff, A. Benamor, M.S. Nasser, E. Mahmoudi, A.W. Mohammad, Synthesis and characterization of Sm3+-doped ZnO nanoparticles via a sol–gel method and their photocatalytic application. J. Sol-Gel. Sci. Technol. **85**, 178–190 (2018). https://doi.org/10.1007/s10971-017-4503-z
25. Huang MH, Wu Y, Feick H, Tran N, Weber E, Yang P (2001) Catalytic Growth of Zinc Oxide Nanowires by Vapor Transport. Adv Mater 13:113–116. https://doi.org/10.1002/1521-4095(200101)13:2<113::AID-ADMA113>3.0.CO;2-H
26. W.I. Park, D.H. Kim, S.W. Jung, G.C. Yi, Metalorganic vapor-phase epitaxial growth of vertically well-aligned ZnO nanorods. Appl. Phys. Lett. **80**, 4232–4234 (2002). https://doi.org/10.1063/1.1482800
27. D. Chen, X. Jiao, G. Cheng, Hydrothermal synthesis of zinc oxide powders with different morphologies. Solid State Commun. **113**, 363–366 (1999). https://doi.org/10.1016/s0038-1098(99)00472-x
28. M. Ristić, S. Musić, M. Ivanda, S. Popović, Sol-gel synthesis and characterization of nanocrystalline ZnO powders. J. Alloys Compd. **397**, 4–7 (2005). https://doi.org/10.1016/j.jallcom.2005.01.045
29. W.T. Chiou, W.Y. Wu, J.M. Ting, Growth of single crystal ZnO nanowires using sputter deposition. Diam Relat Mater **12**, 1841–1844 (2003). https://doi.org/10.1016/S0925-9635(03)00274-7
30. I. Jellal, K. Nouneh, H. Toura, M. Boutamart, S. Briche, J. Naja, B.M. Soucase, M.E. Touhami, Enhanced photocatalytic activity of supported Cu-doped ZnO nanostructures prepared by SILAR method. Opt. Mater. (Amst) **111**, 110669 (2021). https://doi.org/10.1016/J.OPTMAT.2020.110669
31. A. Kolodziejczak-Radzimska, T. Jesionowski, Zinc oxide-from synthesis to application: A review. Materials (Basel) **7**, 2833–2881 (2014). https://doi.org/10.3390/ma7042833
32. K. Hayat, M.A. Gondal, M.M. Khaled, S. Ahmed, A.M. Shemsi, Nano ZnO synthesis by modified sol gel method and its application in heterogeneous photocatalytic removal of phenol from water. Appl Catal A Gen **393**, 122–129 (2011). https://doi.org/10.1016/j.apcata.2010.11.032
33. M. Khuili, N. Fazouan, H. Abou El Makarim, E.H. Atmani, D.P. Rai, M. Houmad, First-principles calculations of rare earth (RE=Tm, Yb, Ce) doped ZnO: Structural, optoelectronic, magnetic, and electrical properties. Vacuum **181**, 109603 (2020). https://doi.org/10.1016/J.VACUUM.2020.109603
34. R. Ahsan, A. Mitra, S. Omar, M.Z. Rahman Khan, M.A. Basith, Sol-gel synthesis of DyCrO3 and 10% Fe-doped DyCrO3 nanoparticles with enhanced photocatalytic hydrogen production abilities. RSC Adv **8**, 14258–14267 (2018). https://doi.org/10.1039/c8ra01585f
35. M.A. Basith, R. Ahsan, I. Zarin, M.A. Jalil, Enhanced photocatalytic dye degradation and hydrogen production ability of Bi25FeO40-rGO nanocomposite and mechanism insight. Sci Rep **8**, 33–35 (2018). https://doi.org/10.1038/s41598-018-29402-w

36. A.M. Tama, S. Das, S. Dutta, M.D.I. Bhuyan, M.N. Islam, M.A. Basith, MoS2 nanosheet incorporated α-Fe2O3/ZnO nanocomposite with enhanced photocatalytic dye degradation and hydrogen production ability. RSC Adv **9**, 40357–40367 (2019). https://doi.org/10.1039/c9ra07526g
37. S. Science (2019) Ce Pte Us Pt. Mater Res Express 0–12
38. P. Giannozzi, S. Baroni, N. Bonini, M. Calandra, R. Car, C. Cavazzoni, D. Ceresoli, G.L. Chiarotti, M. Cococcioni, I. Dabo, A. Dal Corso, S. De Gironcoli, S. Fabris, G. Fratesi, R. Gebauer, U. Gerstmann, C. Gougoussis, A. Kokalj, M. Lazzeri, L. Martin-Samos, N. Marzari, F. Mauri, R. Mazzarello, S. Paolini, A. Pasquarello, L. Paulatto, C. Sbraccia, S. Scandolo, G. Sclauzero, A.P. Seitsonen, A. Smogunov, P. Umari, R.M. Wentzcovitch, QUANTUM ESPRESSO: A modular and open-source software project for quantum simulations of materials. J. Phys. Condens. Matter (2009). https://doi.org/10.1088/0953-8984/21/39/395502
39. G. Kresse, J. Furhmuller (1993) V.A.S.P. Software, Vienna (1999); Kresse G. and Hafner. Phys Rev B 47:R558
40. J. Paier, R. Hirschl, M. Marsman, G. Kresse (2005) The Perdew-Burke-Ernzerhof exchange-correlation functional applied to the G2-1 test set using a plane-wave basis set. J. Chem. Phys. 122:. https://doi.org/10.1063/1.1926272
41. V.I. Anisimov, J. Zaanen, O.K. Andersen, Band theory and Mott insulators: Hubbard U instead of Stoner I. Phys. Rev. B **44**, 943–954 (1991). https://doi.org/10.1103/PhysRevB.44.943
42. H. Hsu, P. Blaha, R.M. Wentzcovitch, C. Leighton (2010) Cobalt spin states and hyperfine interactions in LaCoO3 investigated by LDA+U calculations. Phys Rev B - Condens Matter Mater Phys 82:. https://doi.org/10.1103/PhysRevB.82.100406
43. H. Hsu, K. Umemoto, M. Cococcioni, R. Wentzcovitch (2009) First-principles study for low-spin LaCoO3 with a structurally consistent Hubbard U. Phys Rev B - Condens Matter Mater Phys 79:. https://doi.org/10.1103/PhysRevB.79.125124
44. L. Honglin, L. Yingbo, L. Jinzhu, Y. Ke, Experimental and first-principles studies of structural and optical properties of rare earth (RE = La, Er, Nd) doped ZnO. J. Alloys Compd. **617**, 102–107 (2014). https://doi.org/10.1016/j.jallcom.2014.08.019
45. X. Ma, Y. Wu, Y. Lv, Y. Zhu, Correlation effects on lattice relaxation and electronic structure of zno within the GGA+ U formalism. J. Phys. Chem. C **117**, 26029–26039 (2013). https://doi.org/10.1021/jp407281x
46. A. Phuruangrat, O. Yayapao, T. Thongtem, S. Thongtem, Preparation, characterization and photocatalytic properties of Ho doped ZnO nanostructures synthesized by sonochemical method. Superlattices Microstruct. **67**, 118–126 (2014). https://doi.org/10.1016/j.spmi.2013.12.023
47. C.C. Lin, S.L. Young, C.Y. Kung, L. Horng, H.Z. Chen, M.C. Kao, Y.T. Shih, C.R. Ou, Phonon spectra and magnetic behaviors of hydrothermally synthesized Sm-doped ZnO nanorods. Vacuum **87**, 178–181 (2013). https://doi.org/10.1016/j.vacuum.2012.04.010
48. S.A. Ansari, A. Nisar, B. Fatma, W. Khan, A.H. Naqvi, Investigation on structural, optical and dielectric properties of Co doped ZnO nanoparticles synthesized by gel-combustion route. Mater Sci Eng B

Solid-State Mater Adv Technol **177**, 428–435 (2012). https://doi.org/10.1016/j.mseb.2012.01.022

49. A. Vanaja, G.V. Ramaraju, K. Srinivasa Rao (2016) Structural and optical investigation of Al doped ZnO nanoparticles synthesized by Sol-gel process. Indian J Sci Technol 9:. https://doi.org/10.17485/ijst/2016/v9i12/87013
50. C. Suryanarayana, M.G. Norton (1998) X-Rays and Diffraction. X-Ray Diffr 3–19. https://doi.org/10.1007/978-1-4899-0148-4_1
51. S.S. Chowdhury, A.H.M. Kamal, R. Hossain, M. Hasan, M.F. Islam, B. Ahmmad, M.A. Basith, Dy doped BiFeO3: A bulk ceramic with improved multiferroic properties compared to nano counterparts. Ceram. Int. **43**, 9191–9199 (2017). https://doi.org/10.1016/j.ceramint.2017.04.072
52. M.A. Basith, M.A. Islam, B. Ahmmad, M.D. Sarowar Hossain, K. Mølhave (2017) Preparation of high crystalline nanoparticles of rare-earth based complex pervoskites and comparison of their structural and magnetic properties with bulk counterparts. Mater Res Express 4:. https://doi.org/10.1088/2053-1591/aa769e
53. J.C. Sin, S.M. Lam, K.T. Lee, A.R. Mohamed, Photocatalytic performance of novel samarium-doped spherical-like ZnO hierarchical nanostructures under visible light irradiation for 2,4-dichlorophenol degradation. J. Colloid Interface Sci. **401**, 40–49 (2013). https://doi.org/10.1016/j.jcis.2013.03.043
54. A.L. Patterson, The scherrer formula for X-ray particle size determination. Phys Rev **56**, 978–982 (1939). https://doi.org/10.1103/PhysRev.56.978
55. Z. Tang, N.A. Kotov, M. Giersig, Spontaneous organization of single CdTe nanoparticles into luminescent nanowires. Science **297**, 237–240 (2002). https://doi.org/10.1126/science.1072086
56. G.M. Rai, M.A. Iqbal, Y. Xu, I.G. Will, W. Zhang, Influence of rare earth Ho3+ doping on structural, microstructure and magnetic properties of ZnO bulk and thin film systems. Chinese J Chem Phys **24**, 353–357 (2011). https://doi.org/10.1088/1674-0068/24/03/353-357
57. V. Štengl, S. Bakardjieva, N. Murafa, Preparation and photocatalytic activity of rare earth doped TiO2 nanoparticles. Mater Chem Phys **114**, 217–226 (2009). https://doi.org/10.1016/j.matchemphys.2008.09.025
58. J.C. Sin, S.M. Lam, K.T. Lee, A.R. Mohamed, Preparation and photocatalytic properties of visible light-driven samarium-doped ZnO nanorods. Ceram. Int. **39**, 5833–5843 (2013). https://doi.org/10.1016/j.ceramint.2013.01.004
59. M.L. Myrick, M.N. Simcock, M. Baranowski, H. Brooke, S.L. Morgan, J.N. McCutcheon, The kubelka-munk diffuse reflectance formula revisited. Appl. Spectrosc. Rev. **46**, 140–165 (2011). https://doi.org/10.1080/05704928.2010.537004
60. R. Mahdavi, S.S.A. Talesh, Sol-gel synthesis, structural and enhanced photocatalytic performance of Al doped ZnO nanoparticles. Adv Powder Technol **28**, 1418–1425 (2017). https://doi.org/10.1016/j.apt.2017.03.014
61. T.S. Moss, The Interpretation of the Properties of Indium Antimonide. Proc Phys Soc Sect B **67**, 775 (1954). https://doi.org/10.1088/0370-1301/67/10/306

62. A. Franco, H.V. Pessoni, Optical band-gap and dielectric behavior in Ho - Doped ZnO nanoparticles. Mater Lett **180**, 305–308 (2016). https://doi.org/10.1016/j.matlet.2016.04.170
63. A. Layek, S. Banerjee, B. Manna, A. Chowdhury, Synthesis of rare-earth doped ZnO nanorods and their defect-dopant correlated enhanced visible-orange luminescence. RSC Adv **6**, 35892–35900 (2016). https://doi.org/10.1039/c6ra02278b
64. S.A. Ayon, M.M. Billah, S.S. Nishat, A. Kabir, Enhanced photocatalytic activity of Ho3+ doped ZnO NPs synthesized by modified sol-gel method: An experimental and theoretical investigation. J. Alloys Compd. **856**, 158217 (2021). https://doi.org/10.1016/j.jallcom.2020.158217
65. K.J. Chen, T.H. Fang, F.Y. Hung, L.W. Ji, S.J. Chang, S.J. Young, Y.J. Hsiao, The crystallization and physical properties of Al-doped ZnO nanoparticles. Appl Surf Sci **254**, 5791–5795 (2008). https://doi.org/10.1016/j.apsusc.2008.03.080
66. Y. Liang, N. Guo, L. Li, R. Li, G. Ji, S. Gan, Preparation of porous 3D Ce-doped ZnO microflowers with enhanced photocatalytic performance. RSC Adv **5**, 59887–59894 (2015). https://doi.org/10.1039/c5ra08519e
67. A.R. Khantoul, M. Sebais, B. Rahal, B. Boudine, O. Halimi, Structural and optical properties of zno and co doped ZnO thin films prepared by sol-gel. Acta Phys Pol A **133**, 114–117 (2018). https://doi.org/10.12693/APhysPolA.133.114
68. M.M. Ba-Abbad, M.S. Takriff, A. Benamor, M.S. Nasser, E. Mahmoudi, A.W. Mohammad, Synthesis and characterization of Sm3+-doped ZnO nanoparticles via a sol–gel method and their photocatalytic application. J. Sol-Gel. Sci. Technol. **85**, 178–190 (2018). https://doi.org/10.1007/s10971-017-4503-z
69. D.D. Wang, G.Z. Xing, J.H. Yang, L.L. Yang, M. Gao, J. Cao, Y.J. Zhang, B. Yao, Dependence of energy transfer and photoluminescence on tailored defects in Eu-doped ZnO nanosheets-based microflowers. J. Alloys Compd. **504**, 22–26 (2010). https://doi.org/10.1016/J.JALLCOM.2010.05.105
70. G. Dufour, R.C. Karnatak, J.M. Mariot, C. Bonnelle, Atomic and chemical effects in Sm and Sm2O3 photoelectron spectra. Chem. Phys. Lett. **42**, 433–436 (1976). https://doi.org/10.1016/0009-2614(76)80646-X
71. T.-D. Nguyen, C.-T. Dinh, T.-O. Do, Monodisperse Samarium and Cerium Orthovanadate Nanocrystals and Metal Oxidation States on the Nanocrystal Surface. Langmuir **25**, 11142–11148 (2009). https://doi.org/10.1021/LA901387Q
72. H. Liu, G. Liu, Q. Zhou, G. Xie, Z. Hou, M. Zhang, Z. He, Preparation and photocatalytic activity of Gd3+-doped trititanate nanotubes. Microporous Mesoporous Mater. **142**, 439–443 (2011). https://doi.org/10.1016/j.micromeso.2010.11.035
73. N. Guettaï, H. Ait Amar, Photocatalytic oxidation of methyl orange in presence of titanium dioxide in aqueous suspension. Part II: Kinetics study. Desalination **185**, 439–448 (2005). https://doi.org/10.1016/j.desal.2005.04.049

74. W. Ben Haj Othmen, M. Ben Ali, W. Bouslama, H. Elhouichet, Solar driven photocatalytic properties of Sm3+ doped ZnO nanocrystals. Ceram. Int. **46**, 18878–18887 (2020). https://doi.org/10.1016/j.ceramint.2020.04.208
75. J.C. Sin, S.M. Lam, K.T. Lee, A.R. Mohamed, Preparation of rare earth-doped ZnO hierarchical micro/nanospheres and their enhanced photocatalytic activity under visible light irradiation. Ceram. Int. **40**, 5431–5440 (2014). https://doi.org/10.1016/j.ceramint.2013.10.128
76. G.Y. Yao, G.H. Fan, F. Zhao, J.H. Ma, J. Chen, S.W. Zheng, S.M. Zeng, L.F. He, T. Zhang, In assisted realization of p-type C-doped ZnO: A first-principles study. Phys B Condens Matter **407**, 3539–3542 (2012). https://doi.org/10.1016/J.PHYSB.2012.05.019

Figures

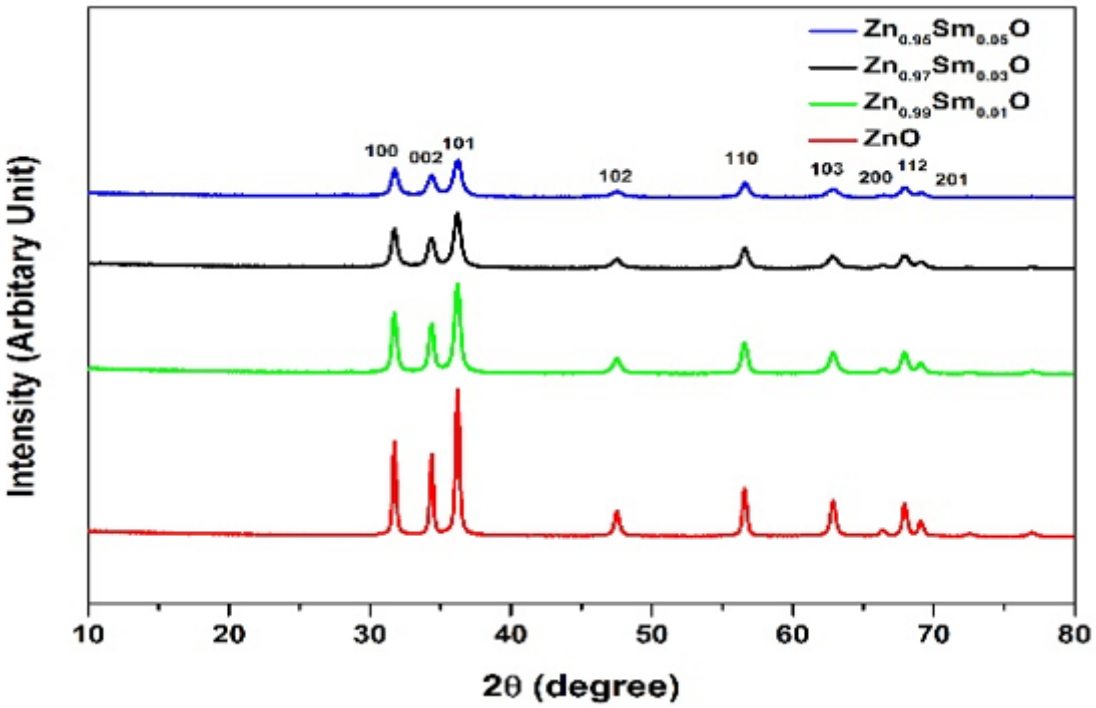

Figure 1

Reduction in XRD peak intensity with increasing Sm3+ concentration

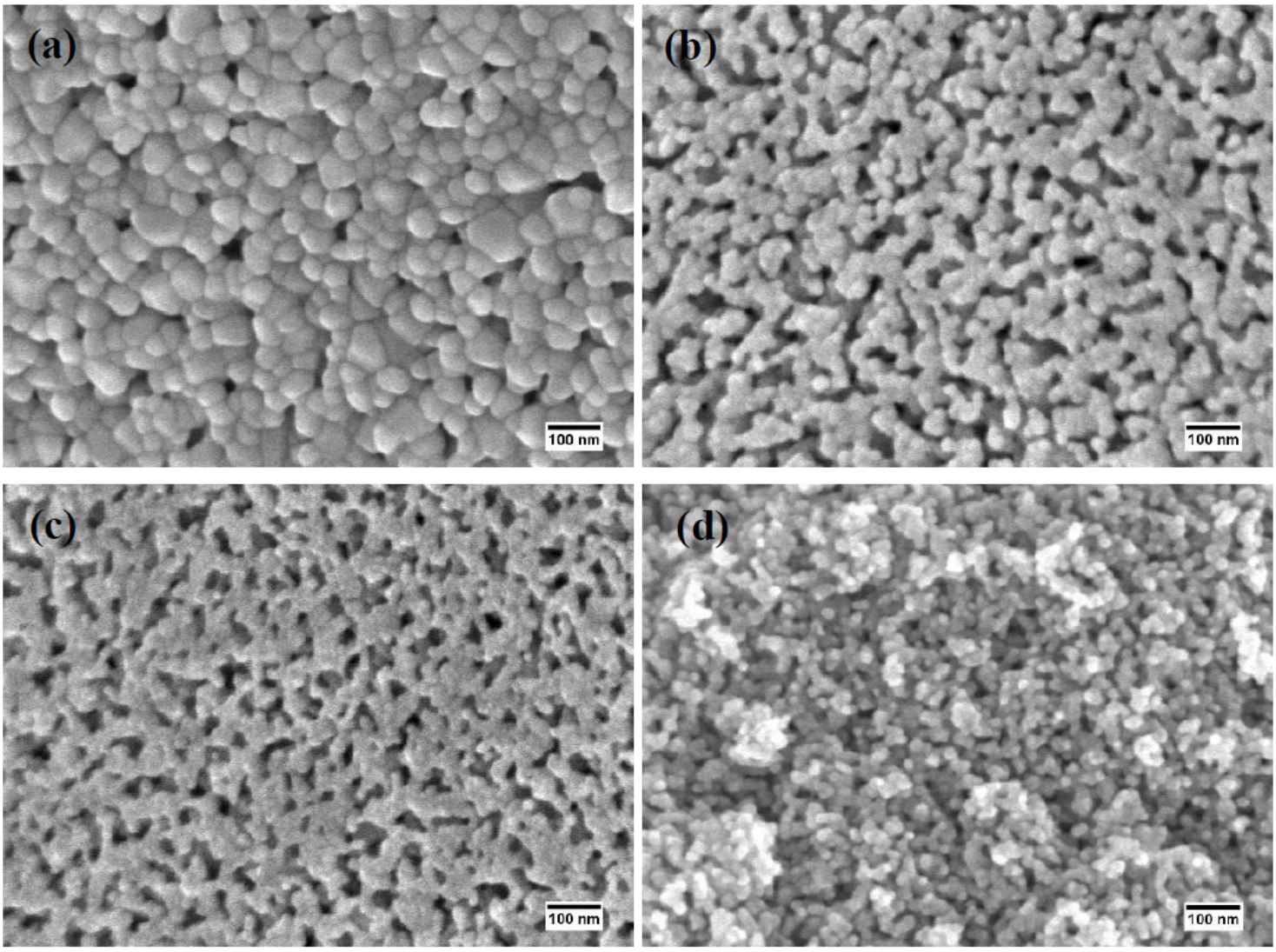

Figure 2

FESEM micrographs of (a) undoped, (b) Zn0.99Sm0.01O, (c) Zn0.97Sm0.03O and (d) Zn0.95Sm0.05O NPs showing morphological changes

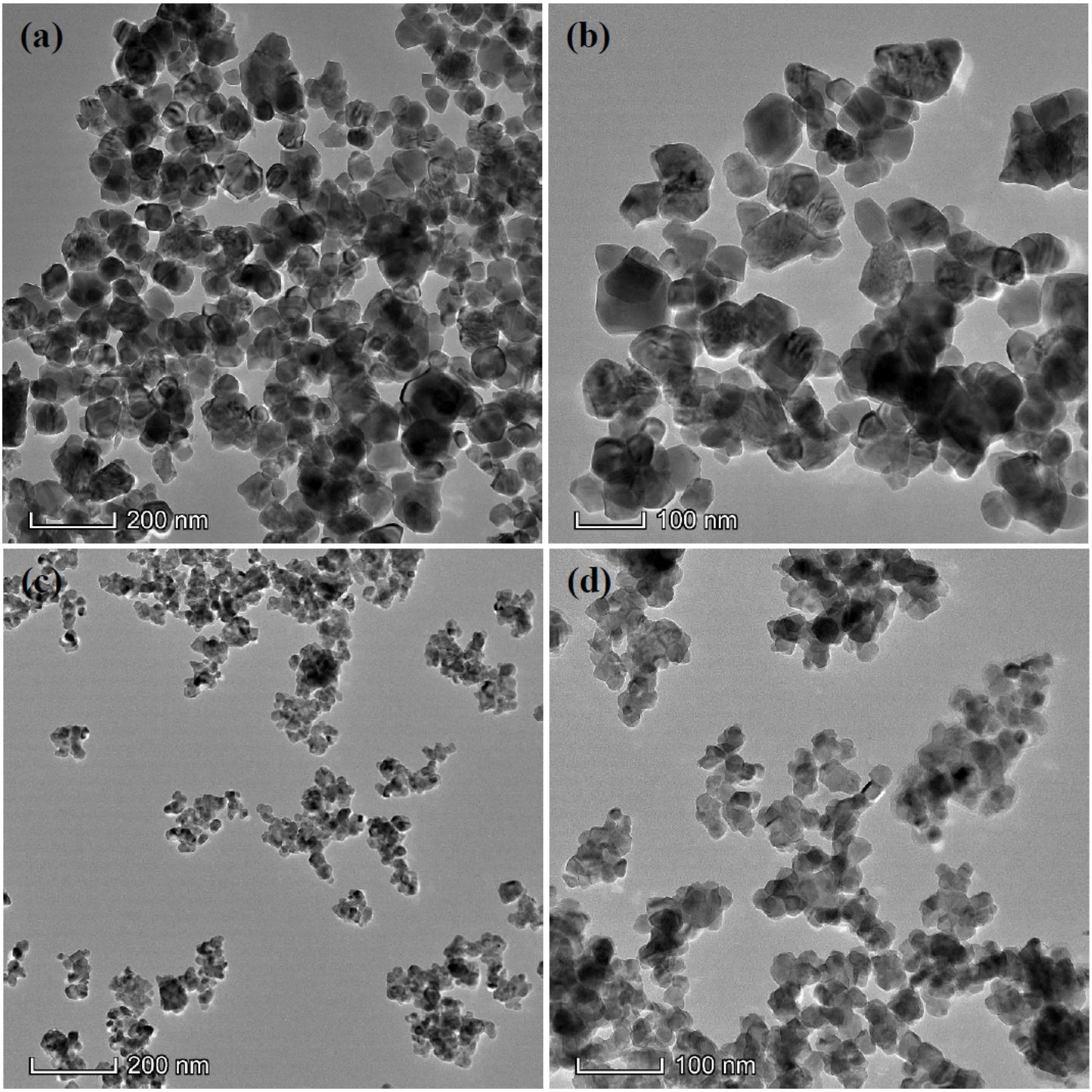

Figure 3

TEM images of (a), (b) ZnO and (c), (d) Zn0.97Sm0.03O exhibiting reduced particle size on doing.

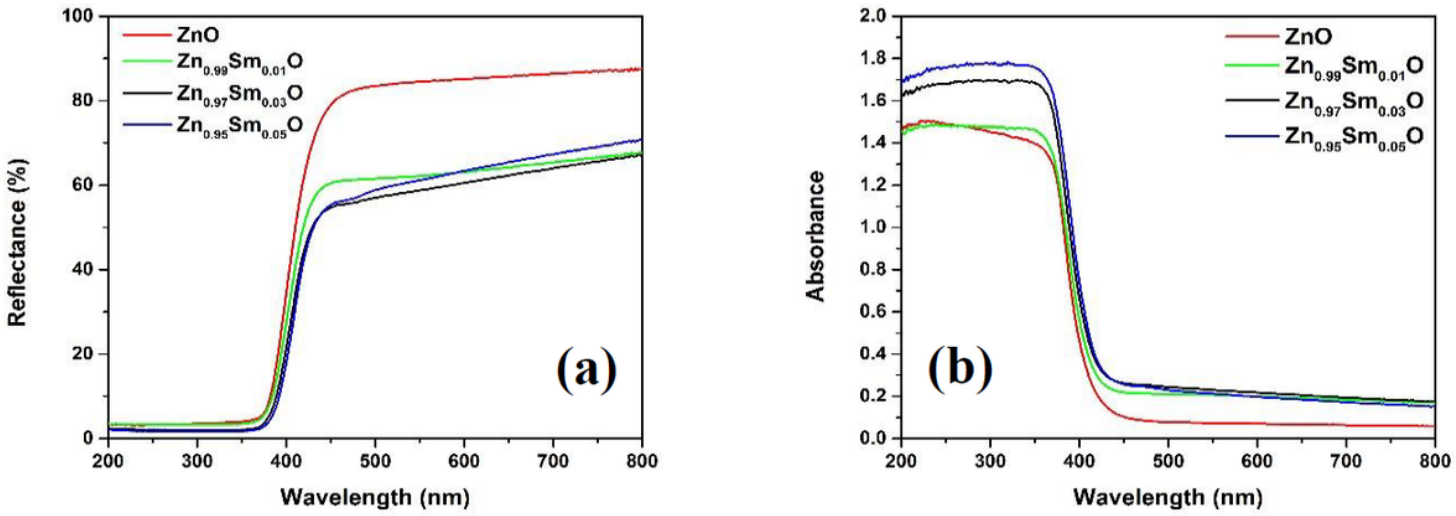

Figure 4

Curve of (a) reflectance and (b) absorbance variation from UV-vis DRS spectra

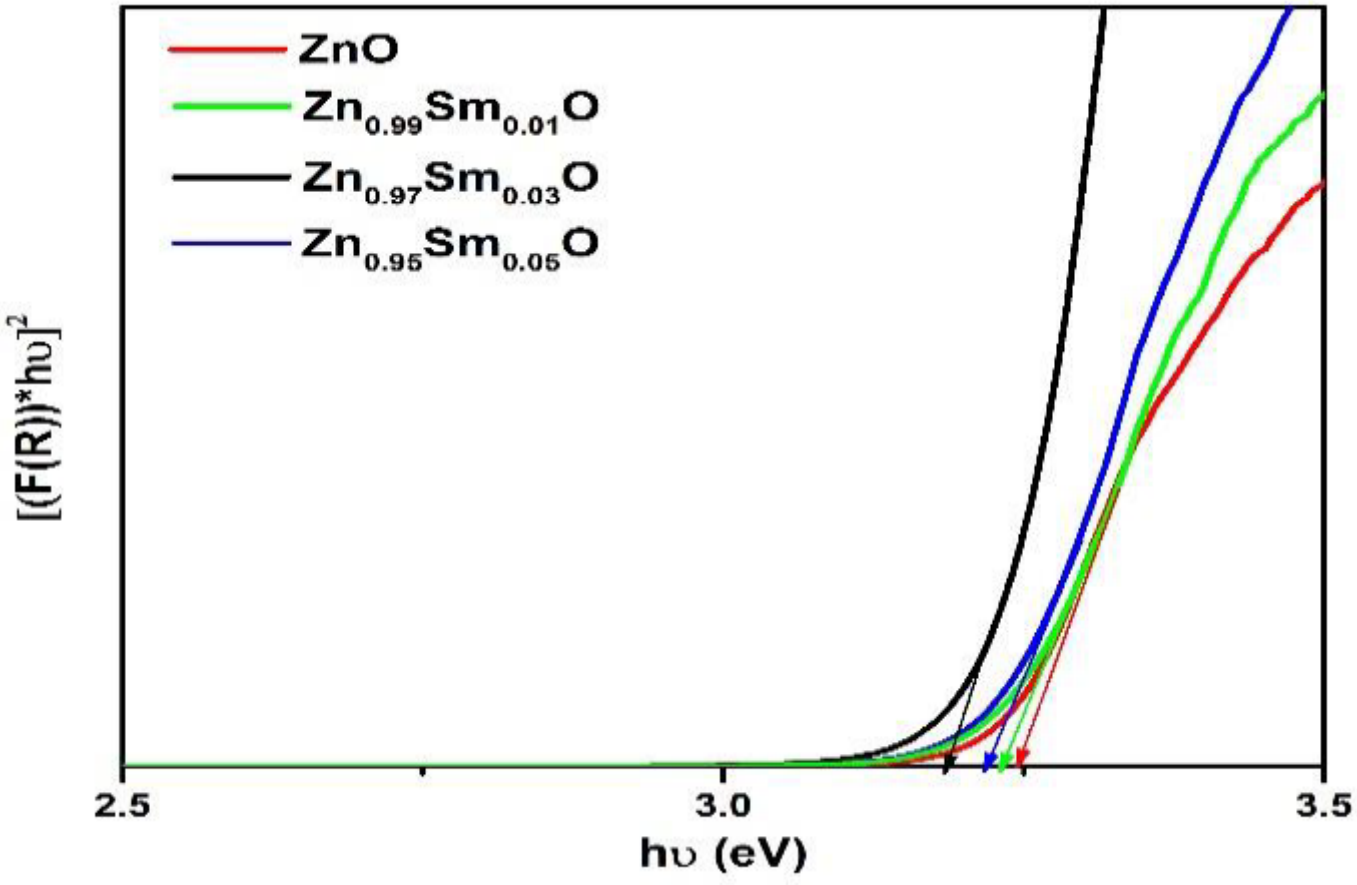

Figure 5

Optical band gap variation with increasing doping amount calculated using UV-vis DRS spectra using Kulbelka-Muck function

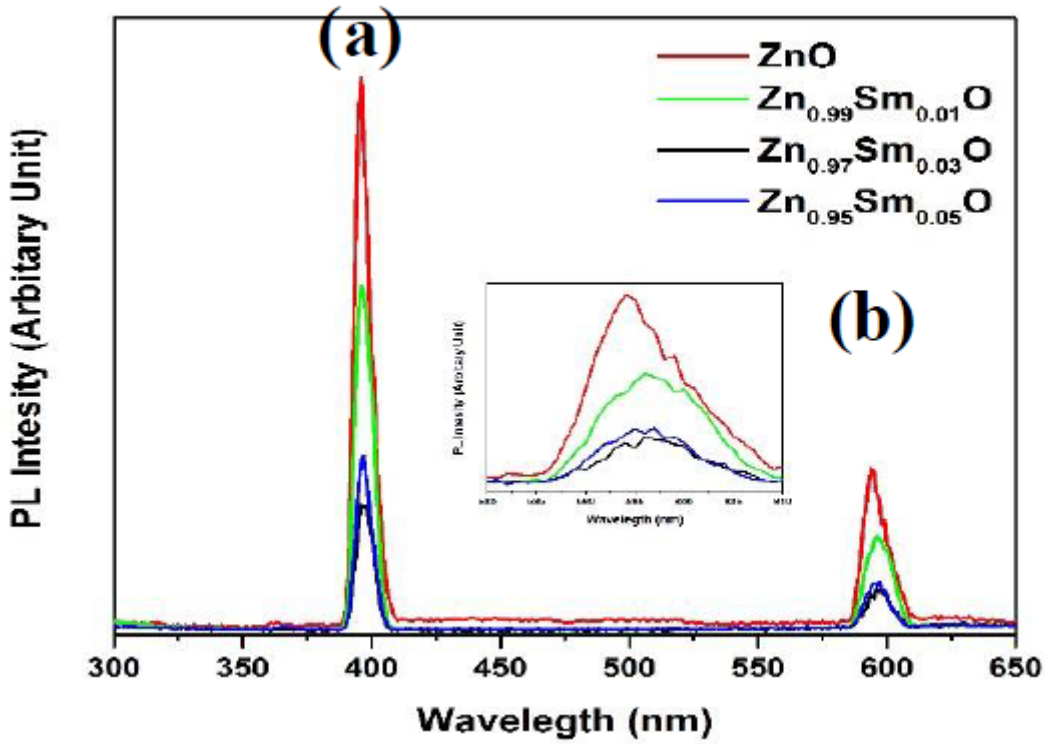

Figure 6

Photoluminescence spectra exhibiting (a) near band gap emission and (b) orange luminescence.

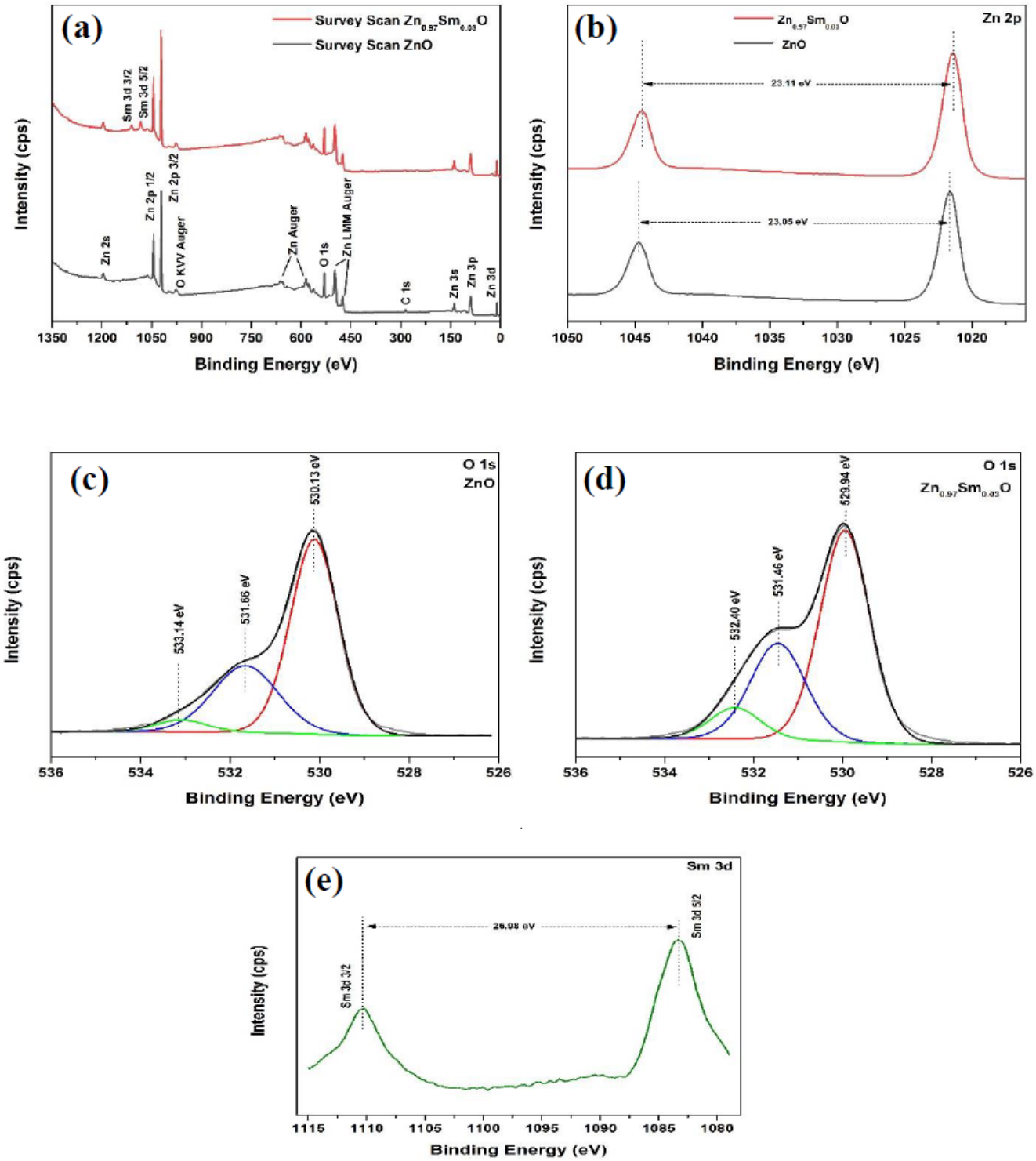

Figure 7

(a) XPS survey spectra of ZnO and Zn0.97Sm0.03O, (b) High resolution scans of Zn 2P of ZnO and Zn0.97Sm0.03O, (c) High resolution scan with deconvolution of O 1s of ZnO, (d) High resolution scan with deconvolution of O 1s of Zn0.97Sm0.03O and (e) High resolution scan of Sm 3d of Zn0.97Sm0.03O.

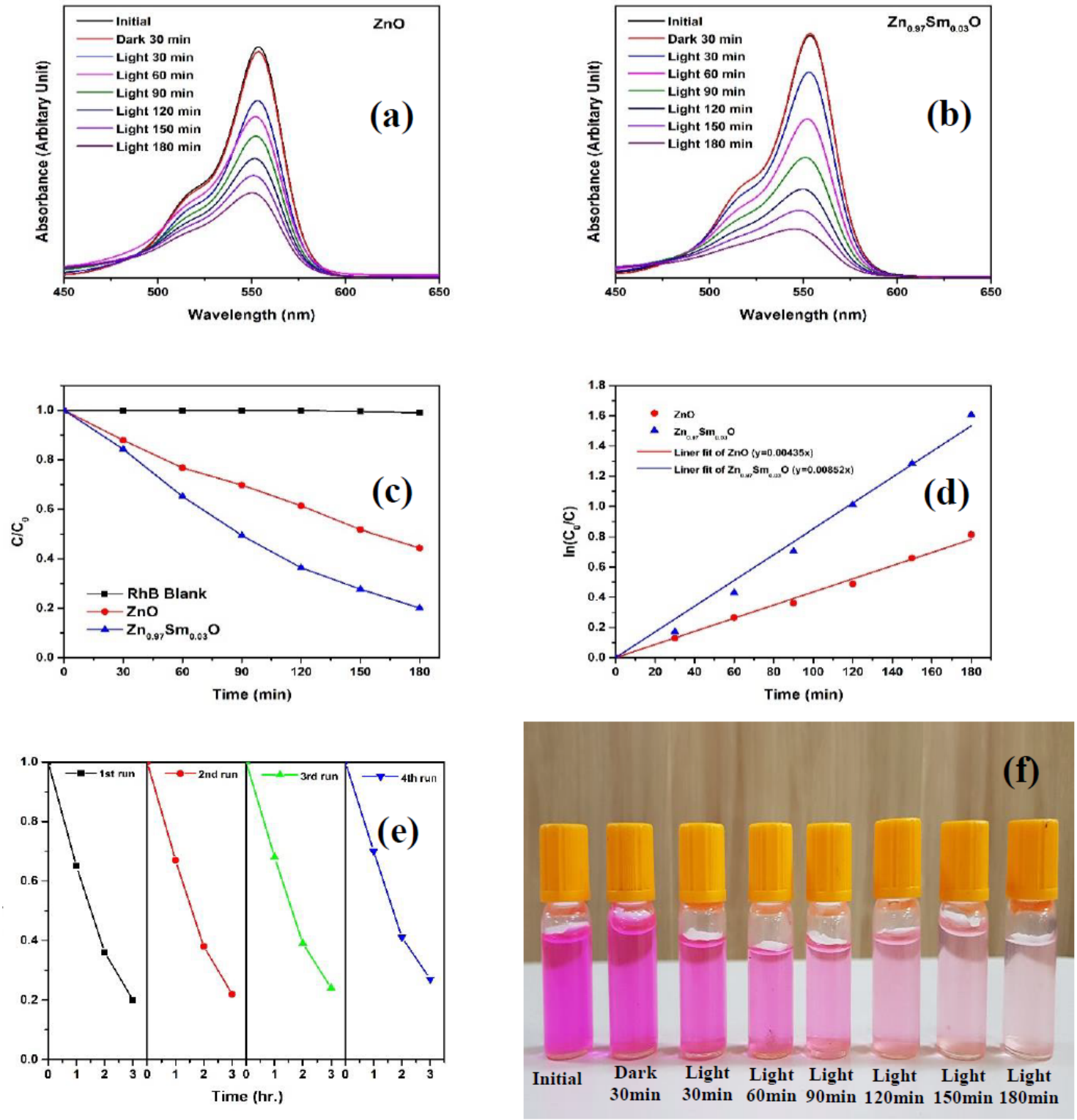

Figure 8

(a) absorption spectra of RhB with ZnO suspension, (b) absorption spectra of RhB with Zn0.97Sm0.03O suspension, (c) RhB degradation for blank, pristine and Zn0.97Sm0.03O, (d) degradation rate constant, k, (e) reusability of Zn0.97Sm0.03O for 4 consecutive runs and (f) Visual illustration of RhB degradation in the presence of Zn0.97Sm0.03O.

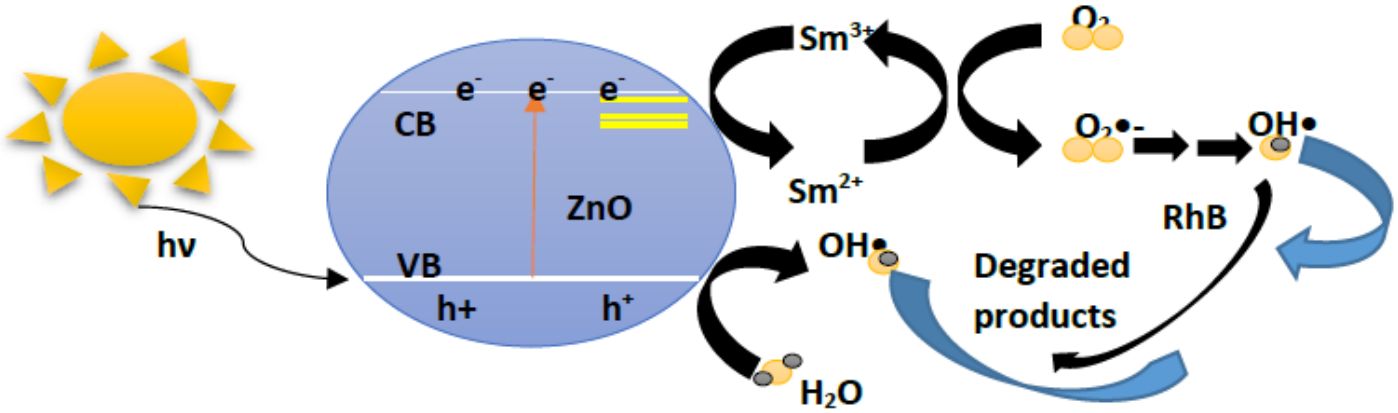

Figure 9

Proposed Photocatalytic Mechanism of Sm3+ doped ZnO

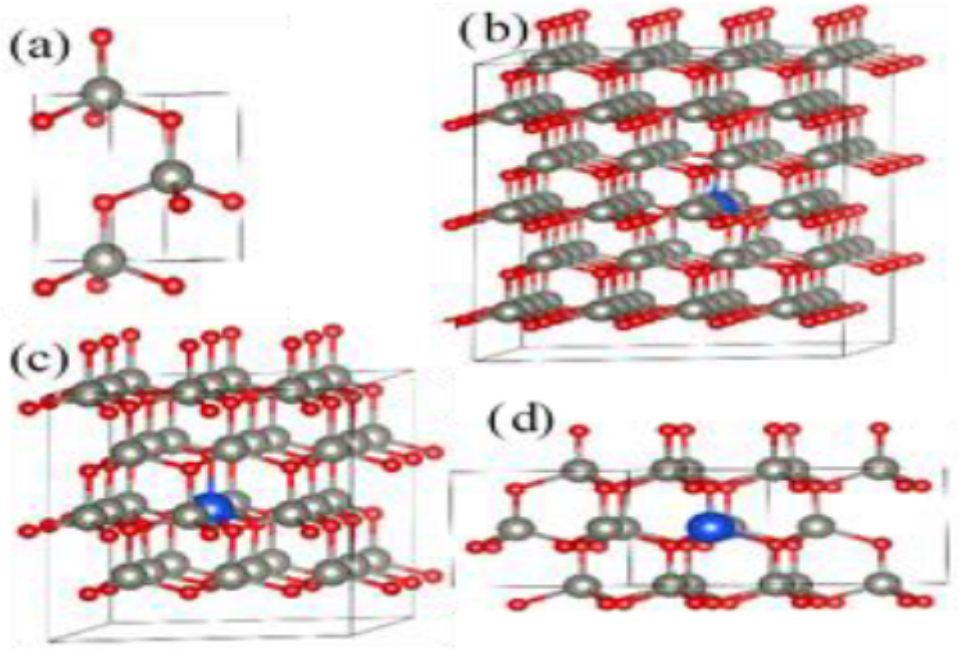

Figure 10

(a) ZnO unit cell, (b)-(e) 1.04, 2.8 and 5.5 mole percent Sm3+ doped ZnO supercell, respectively. Zn2+ are represents with gray balls, O2- with red balls and Sm3+ with blue balls.

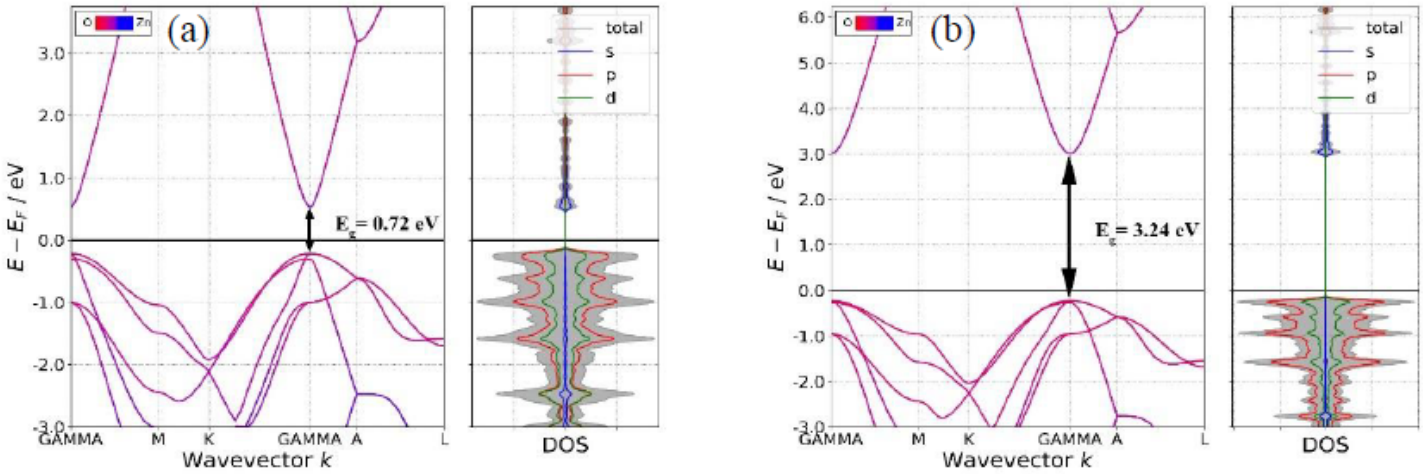

Figure 11

Band structure of pure ZnO using (a) DFT approximation and (b) DFT+U approximation.

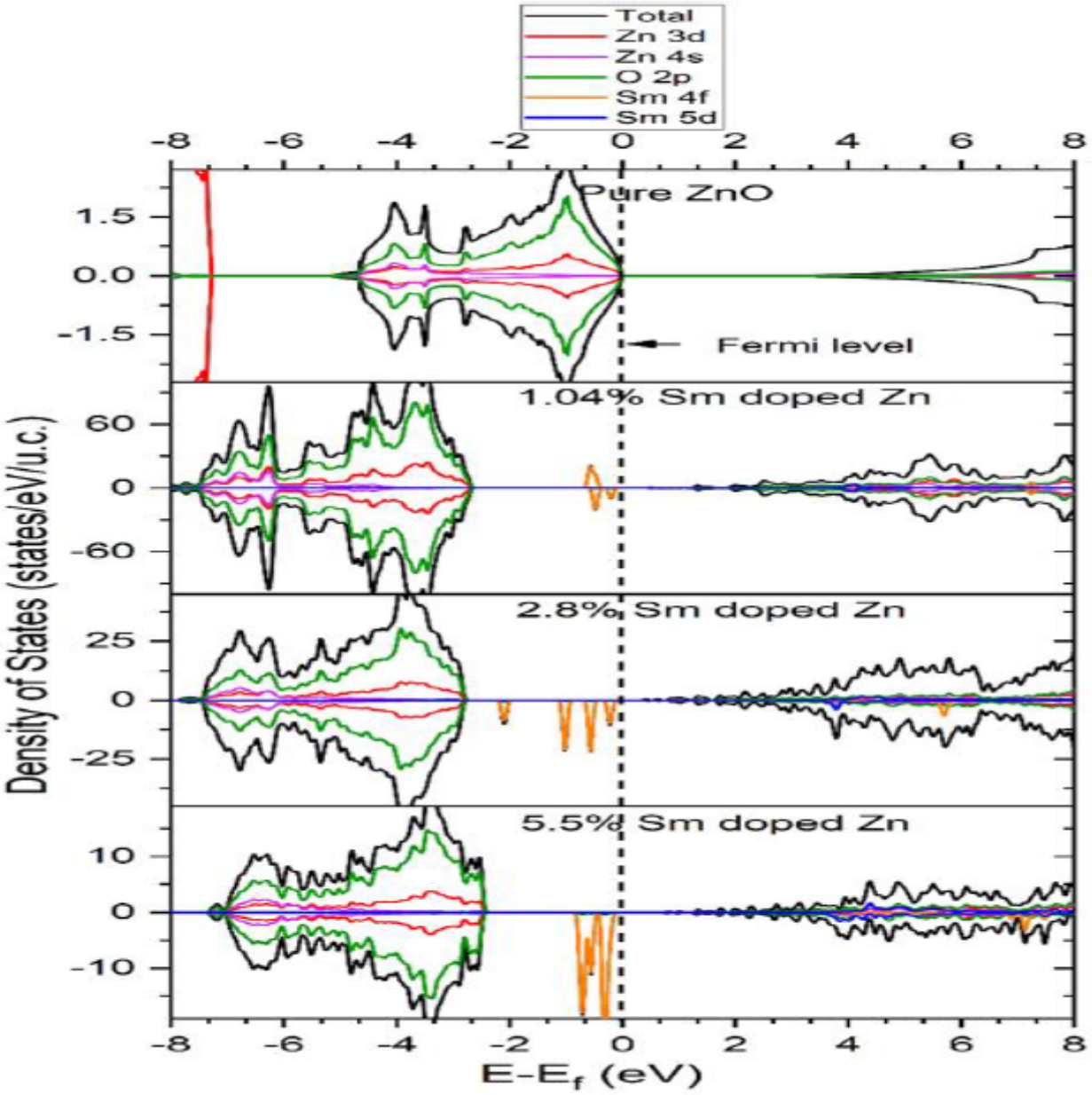

Figure 12

Projected density of states for pristine and Sm3+ doped ZnO.

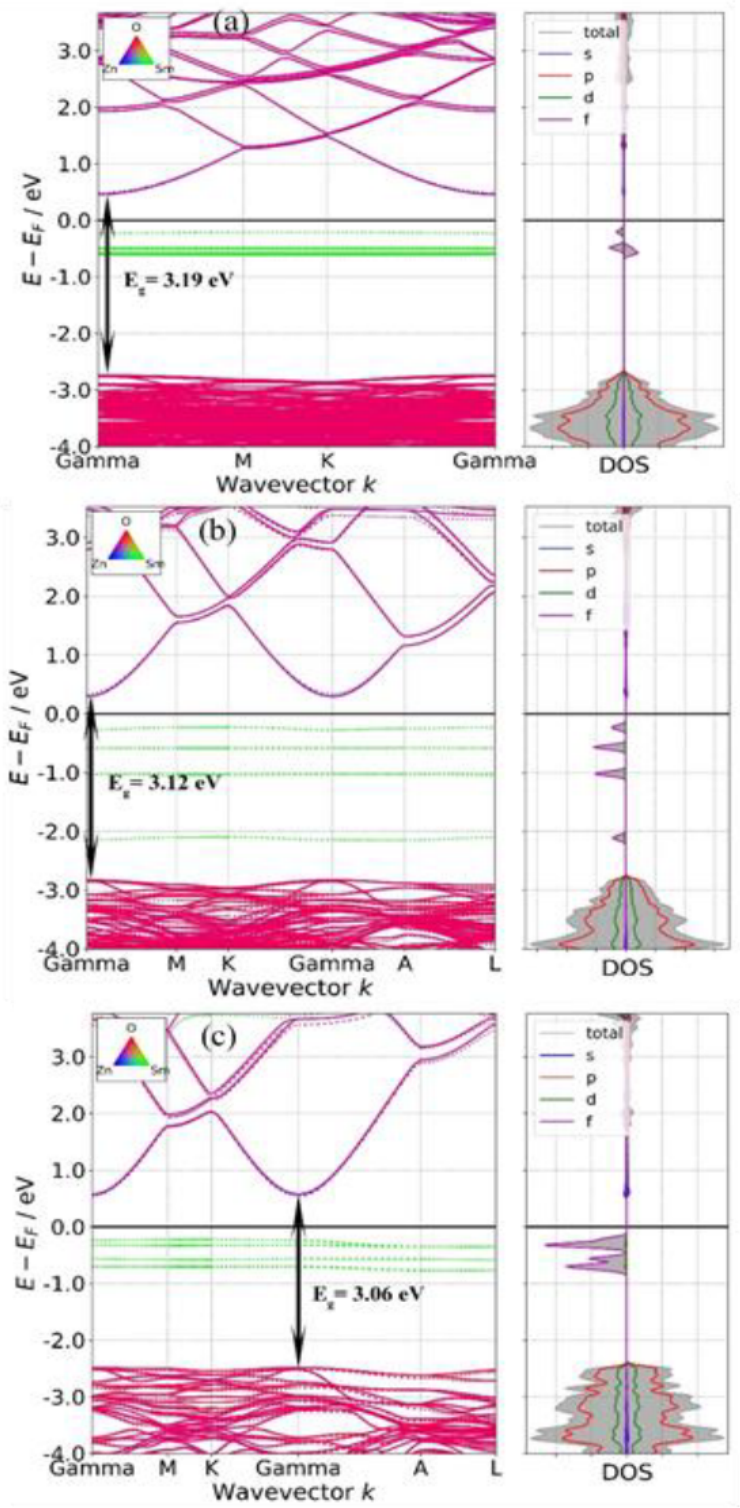

Figure 13

Band structure of (a) 1.04 (b) 2.8 and (c) 5.5 mole percent Sm3+ dopped ZnO.